

Structural and chemical orders in $\text{Ni}_{64.5}\text{Zr}_{35.5}$ metallic glass by molecular dynamics simulation

L. Tang,^{1,2} T. Q. Wen,^{2,3} N. Wang,^{3,*} Y. Sun,² F. Zhang,² Z. J. Yang,^{1,2} K. M. Ho,^{2,4} and C. Z. Wang^{2,4,*}

¹Department of Applied Physics, College of Science, Zhejiang University of Technology, Hangzhou 310023, China

²Ames Laboratory-USDOE, Iowa State University, Ames, Iowa 50011, USA

³MOE Key Laboratory of Materials Physics and Chemistry under Extraordinary Conditions, School of Natural and Applied Sciences, Northwestern Polytechnical University, Xi'an 710072, China

⁴Department of Physics and Astronomy, Iowa State University, Ames, Iowa 50011, USA



(Received 14 September 2017; revised manuscript received 26 December 2017; published 6 March 2018)

The atomic structure of $\text{Ni}_{64.5}\text{Zr}_{35.5}$ metallic glass has been investigated by molecular dynamics (MD) simulations. The calculated structure factors from the MD glassy sample at room temperature agree well with the x-ray diffraction (XRD) and neutron diffraction (ND) experimental data. Using the pairwise cluster alignment and clique analysis methods, we show that there are three types of dominant short-range order (SRO) motifs around Ni atoms in the glass sample of $\text{Ni}_{64.5}\text{Zr}_{35.5}$, i.e., mixed-icosahedron(ICO)-cube, intertwined-cube, and icosahedronlike clusters. Furthermore, chemical order and medium-range order (MRO) analysis show that the mixed-ICO-cube and intertwined-cube clusters exhibit the characteristics of the crystalline B2 phase. Our simulation results suggest that the weak glass-forming ability (GFA) of $\text{Ni}_{64.5}\text{Zr}_{35.5}$ can be attributed to the competition between the glass forming ICO SRO and the crystalline mixed-ICO-cube and intertwined-cube motifs.

DOI: [10.1103/PhysRevMaterials.2.033601](https://doi.org/10.1103/PhysRevMaterials.2.033601)

I. INTRODUCTION

Atomistic structures of metallic glasses (MG) have attracted considerable attention [1–8] since extraordinary properties such as strength and elasticity in MG systems are closely related to the atomic packing structures in the glasses [9]. Although MGs do not exhibit long-range translational and rotational orders, experiments [10–12] and theoretical simulations [13,14] have indicated that there are short- to medium-range orders in MGs. It is believed that the icosahedral (ICO) short-range order (SRO) is responsible for glass-forming ability (GFA) [15–17]. Meanwhile, SRO and medium-range order (MRO) also govern the mechanical response to deformation in the MG systems [18]. Hence investigating such atomic SRO and MRO structures in metallic liquids and glasses is a key to understanding the structure-properties relationship of MG materials.

Among all Ni-Zr alloys with different compositions, it is believed that $\text{Ni}_{64.5}\text{Zr}_{35.5}$ could be the most promising candidate for forming bulk MG, since $\text{Ni}_{64.5}\text{Zr}_{35.5}$ is close to a eutectic point in the Ni-Zr binary phase diagram [19–21]. Because the melting temperature is at a local minimum at the eutectic composition, the kinetics associated with crystal nucleation and growth would be relatively easily suppressed, leading to a relatively higher GFA compared to the same alloy system at other compositions. In particular, it has been shown that the critical cooling rate for glass formation is minimal for the Ni-Zr alloy containing about 35 at.% Zr [22], which suggests that $\text{Ni}_{64.5}\text{Zr}_{35.5}$ has the highest GFA in a Ni-Zr system. However, compared to the well-known Cu-Zr system, which has been commonly regarded as a good glass former in

binary metallic alloys [23,24], experimental synthesis of bulk MG of $\text{Ni}_{64.5}\text{Zr}_{35.5}$ is still very challenging.

Although Ni and Cu differ only by one electron, the GFA of $\text{Cu}_{64.5}\text{Zr}_{35.5}$ and $\text{Ni}_{64.5}\text{Zr}_{35.5}$ is very different. $\text{Cu}_{64.5}\text{Zr}_{35.5}$ glassy samples with mm size can be fabricated by the copper mold casting method [23], while glassy $\text{Ni}_{64.5}\text{Zr}_{35.5}$ ribbons can only be obtained by a careful melt-spinning process [20]. The cooling rate in the melt-spinning method is typically 10^5 – 10^6 K/s, which is much faster (about two orders of magnitude) than that of the casting method. This difference indicates that the GFA of $\text{Ni}_{64.5}\text{Zr}_{35.5}$ is much weaker relative to that of the $\text{Cu}_{64.5}\text{Zr}_{35.5}$ system. This weaker GFA nature of $\text{Ni}_{64.5}\text{Zr}_{35.5}$ could be attributed to the difference in the short- to medium-range order in the atomistic structures between the two systems. For example, it is believed that a crystal-like motif can facilitate the crystal nucleation and growth to prevent the glass formation if the cooling rate is not high enough. Therefore investigating the differences of short- to medium-range ordered structure and chemical order between $\text{Ni}_{64.5}\text{Zr}_{35.5}$ and Cu-Zr system would provide useful insights into the origin of weak GFA in $\text{Ni}_{64.5}\text{Zr}_{35.5}$.

Using the experimental x-ray diffraction (XRD) and neutron diffraction (ND) experimental data, the atomic structure of $\text{Ni}_{64.5}\text{Zr}_{35.5}$ MG has been studied by reverse Monte-Carlo (RMC) method and Voronoi tessellation analysis [25,26]. These studies have suggested that a large number of icosahedral-like and prismatic-like SRO structures exist in $\text{Ni}_{64.5}\text{Zr}_{35.5}$ glass. Moreover, a significant degree of chemical ordering has also been observed in $\text{Ni}_{64.5}\text{Zr}_{35.5}$ glass samples [26]. However, compared to the RMC method, MD simulation has a great advantage in obtaining more reliable atomic structures as long as the interatomic potentials are accurate. Fortunately, the interatomic potential of the Ni-Zr system has been developed recently [27], which allows us to perform direct MD simulations for $\text{Ni}_{64.5}\text{Zr}_{35.5}$. To our knowledge,

*Corresponding authors: nan.wang@nwpu.edu.cn; wangcz@ameslab.gov

although MD simulations for liquid Ni-Zr binary alloys have been reported [27], MD simulations of metallic glass at the composition around $\text{Ni}_{64.5}\text{Zr}_{35.5}$ are still lacking. Moreover, no detailed explanation of experimental results by MD simulations has been reported yet. Reliable MD simulations for this system will enable us to look into the structures of the alloy at undercooled liquid and glass states at the atomistic level, and provide very useful insights into the GFA in this system.

In this paper, the atomic structure of $\text{Ni}_{64.5}\text{Zr}_{35.5}$ glass is studied by MD simulations using the Finnis-Sinclair-type potential recently developed [27,28]. The pairwise cluster alignment method and clique analysis algorithm [29,30] are used to identify the dominant structure order in the MD $\text{Ni}_{64.5}\text{Zr}_{35.5}$ sample. This approach can extract a clique of similar clusters from the atomic structure of the MD sample without knowing the details of packing motif in advance. Meanwhile, the cluster alignment method can also calculate the populations of SRO clusters and explore the MRO in metallic liquid and glass systems. In addition to a large fraction of the intertwined-cube (similar to prismatic-like structure) and icosahedronlike clusters around Ni atoms as previously observed, we found significant populations of Ni-centered mixed-ICO-cube clusters which are composed of half-icosahedron and half-cube in the $\text{Ni}_{64.5}\text{Zr}_{35.5}$ glass sample obtained from the MD simulations. Furthermore, we show that the cubic part of mixed-ICO-cube cluster and the intertwined-cube cluster have excellent chemical ordering, indicating the emergence of a metastable crystalline B2 phase [31]. Our results show that the suppression of glass formation by the crystalline B2 phase could be responsible for the weak GFA of $\text{Ni}_{64.5}\text{Zr}_{35.5}$.

II. METHOD

The sample used in MD simulations of $\text{Ni}_{64.5}\text{Zr}_{35.5}$ contains 3225 Ni and 1775 Zr atoms. The simulations are performed using the isothermal-isobaric (NPT) ensemble with the Nosé-Hoover thermostat in LAMMPS code [28]. The semiempirical Finnis-Sinclair-type interatomic potential developed by Wilson and Mendelev is employed [27]. The time step in the MD simulations is 2.5 fs. Before the cooling process, the sample is held at 2000 K for 2.5 ns to achieve equilibrium. After that, the sample is cooled down to 300 K continuously with different cooling rates at 10^{13} , 10^{12} , 10^{11} , and 10^{10} K/s, respectively. In order to eliminate the effect of atomic thermal motions, the structural and chemical orders in the glass sample at 300 K are averaged over 500 ps, which is sufficient to obtain the convergent results for the structural and physical properties studied in this paper.

In order to compare with the experimental data, the total structure factors $S(q)$ of the $\text{Ni}_{64.5}\text{Zr}_{35.5}$ MD samples are calculated by the Faber-Ziman formalism [32]:

$$S(q) = \sum_{i \leq j} w_{ij} S_{ij}(q), \quad (1)$$

where i or j denotes atomic specie. Here, the partial structure factor $S_{ij}(q)$ is

$$S_{ij}(q) = 1 + 4\pi \rho_j \int_0^\infty [g_{ij}(r) - 1] \frac{\sin(qr)}{r} r dr, \quad (2)$$

where $g_{ij}(r)$ is the partial pair correlation function and ρ_j is the number density of the relevant atom specie. To compare with the XRD results, the q -dependent scattering factors [33]

$$w_{ij}^{\text{XRD}}(q) = (2 - \delta_{ij}) c_i c_j \frac{f_i(q) f_j(q)}{[\sum_i c_i f_i(q)]^2} \quad (3)$$

are used in the Faber-Ziman formalism, where c_i and c_j are the compositions of the relevant atom species and $f_i(q)$ and $f_j(q)$ are the corresponding q -dependent atomic scattering factors in the XRD experiment. For comparison with neutron diffraction (ND) data, we use the weighting coefficients [26]

$$w_{ij}^{\text{ND}} = (2 - \delta_{ij}) c_i c_j \frac{b_i b_j}{(\sum_i c_i b_i)^2}, \quad (4)$$

where b_i and b_j are the coherent neutron scattering length of the relevant atom species [34].

The SROs in $\text{Ni}_{64.5}\text{Zr}_{35.5}$ MD samples are analyzed by the pairwise cluster alignment method [29,30]. In this method, a cluster can be assigned to each atom in the MD sample by extracting this atom and its first neighbor cell atoms along with it from the MD sample. Then, each cluster extracted from the MD sample is used as a template and all other clusters with the same chemical element at the center are aligned against it. The similarity between the aligned cluster and the template is measured by an alignment score defined as

$$f = \min_{0.8 \leq \alpha \leq 1.2} \left[\frac{1}{N} \sum_{i=1}^N \frac{(\vec{r}_{ic} - \alpha \vec{r}_{it})^2}{(\alpha \vec{r}_{it})^2} \right]^{1/2}, \quad (5)$$

where N is the number of the neighbor atoms in the template. \vec{r}_{ic} and \vec{r}_{it} are the atomic positions in the aligned cluster and template, respectively. To obtain optimal alignment α is chosen between 0.8 and 1.2 to vary the size of the template. Once we have all the alignment scores between any two clusters in the glass sample, we can obtain a clique of clusters whose pairwise alignment scores are smaller than a cutoff value of 0.15. The clusters belong to the same clique are very similar with each other and have common SRO.

III. RESULTS AND DISCUSSIONS

Figure 1 shows the evolution of instantaneous potential energy $E - 3k_B T$ as a function of temperature with a continuous cooling rate of 10^{10} K/s. In harmonic systems, the temperature dependence of both kinetic energy and potential energy are $3/2 k_B T$. Therefore $E - 3k_B T$ will be a constant for all temperatures in harmonic systems. By subtracting $3k_B T$ from the total energy obtained from MD simulations, the temperature dependence of anharmonicity in the system can be seen more clearly [35]. In particular, the plot in Fig. 1 shows that the anharmonicity in liquid and glass are different, which enables us to see the glass transition and estimate the glass transition temperature T_g from the plot. From Fig. 1, one can see that at temperature higher than 975 K the energy decreases significantly with decreasing temperature, whereas at the low temperature region with $T < 975$ K the energy has only a slight decrease and is nearly constant around room temperature. Clearly, it shows a transition from liquid to glass

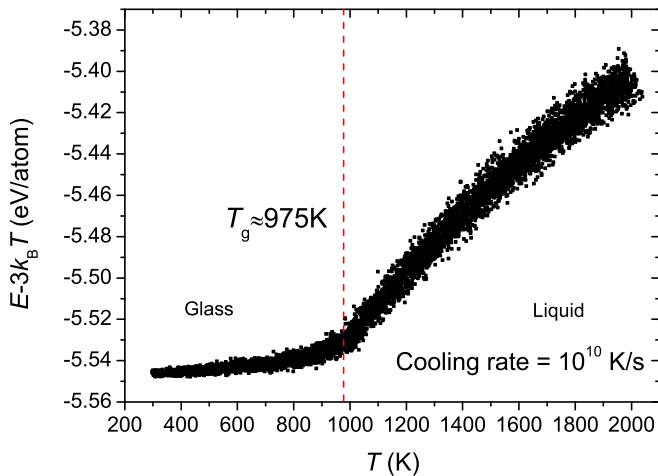


FIG. 1. The instantaneous energy $E - 3k_B T$ as a function of temperature with continuous cooling process, where the cooling rate is 10^{10} K/s. It is clear that there is a phase transition from liquid to glass and the obtained glass transition temperature $T_g \approx 975$ K agrees with the experimental data [19].

and the obtained glass transition temperature is $T_g \approx 975$ K, which agrees with the experimental result [19].

In order to see how good are the glass samples obtained from our MD simulations in comparison with experiment, we calculated the total and partial structure factors using Faber-Ziman formalism [32] for the samples at 300 K prepared by different cooling rates. As shown in Figs. 2(a) and 2(b), although there is a slight shift of the height of the main peak, one can observe that the structure factors calculated from our MD simulations using Eqs. (3) and (4) agree well with the experimental XRD and ND data [26], respectively. It should be noted that as the same problem in RMC method, the agreement between the calculated and experimental $S(q)$ does not always guarantee the correct description of the three-dimensional atomistic structures in the glass sample. Nevertheless, this good agreement of total structure factors is an essential requirement of the reliable MD simulation.

We can see from Figs. 2(a) and 2(b) that the height of main peak increases with lowering cooling rate, indicating that more order is developed with lower cooling rate. In Fig. 2(b), the experimental ND data and the simulated ND spectrum exhibit a prepeak [25] around $q \approx 1.8 \text{ \AA}^{-1}$ in addition to other peaks. Because the low q region in reciprocal space corresponds to large distance in real space, the prepeak would indicate certain medium-range correlations in the glass structure [36]. However, the prepeak is not well seen in the XRD spectra from both experiment and simulation. Therefore the origin of this small prepeak needs further investigation.

The comparisons between the calculated and experimental partial structure factors [26] are shown in Fig. 3. The overall agreement between the calculated and experimental spectra are reasonably good but some discrepancies are present, especially for the partial $S(q)$ of the Zr-Zr pairs. Although the peak positions agree with each other, the peak intensity of the first peak from the calculation is much higher than that seen in experiment. It should be noted that the experimental partial structure factors are calculated from the different total

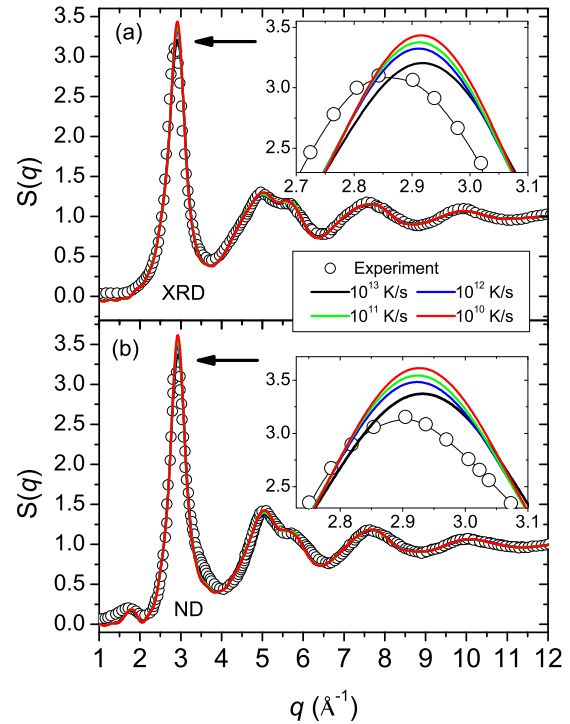


FIG. 2. The comparisons of total structure factors from the MD simulations to the (a) XRD and (b) ND experimental data [26], respectively. One can observe that the calculated total structure factors from MD simulations agree well with the XRD and ND experimental data. The maximal discrepancy between MD simulations and experiments is located at the main peak in low- q region, as shown in the insets. In addition, the ND data from our MD simulation also produce well the characteristic prepeak [25] around $q \approx 1.8 \text{ \AA}^{-1}$, which generally corresponds to medium-range correlations in real space.

structure factors of isotopic substitutions. The differences of total structure factors among the isotopic substitutions may be very small, so that the uncertainty of the obtained partial structure factors could be relatively larger. Another source of the differences may also be attributed to the inaccuracy in the interatomic potential used in the simulation, but we also would like to note that the potential has been successfully applied to explain several phenomena in $\text{Ni}_{50}\text{Zr}_{50}$ (see Ref. [37]). Nevertheless, the main discrepancy is in the intensity of the peak at small q values, which affects the degree of MRO in the system. The peaks of Ni-Ni and Ni-Zr around $q = 3 \text{ (\AA}^{-1})$ corresponding to the dominant SRO clusters in $\text{Ni}_{64.5}\text{Zr}_{35.5}$ agree well with experiment, suggesting the SRO results from our simulation and analysis should be reliable.

The structure analysis based on the atomistic model from our MD simulations shows that the dominant motifs around Ni and Zr atoms in $\text{Ni}_{64.5}\text{Zr}_{35.5}$ glass at 300 K are mixed-ICO-cube, intertwined-cube, and ICO-like clusters. The corresponding structures of mixed-ICO-cube and intertwined-cube motifs are shown in Fig. 4. In mixed-ICO-cube motif, the center Ni atom is surrounded by ten atoms. This motif can be viewed as a combination of a half-cube and a half-icosahedron as shown in Fig. 4(a). The sites (2, 3, 4, 7, 8, 9, 10) are the seven corners of a slightly distorted cube, forming three nearly orthogonal squares. On the other side, the center Ni atom is

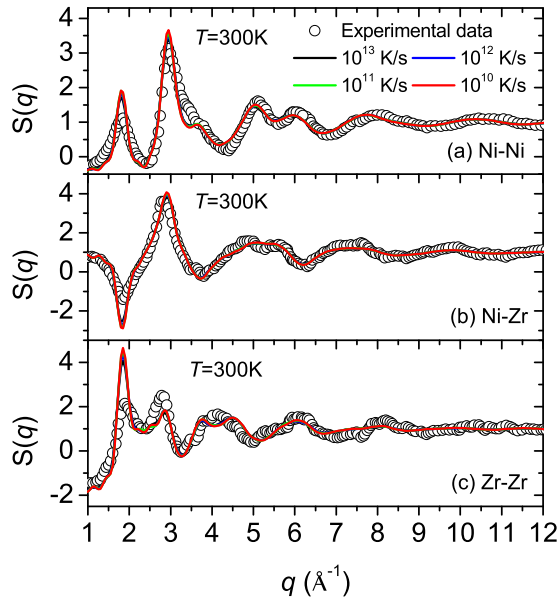


FIG. 3. Partial structure factors of (a) Ni-Ni, (b) Ni-Zr, and (c) Zr-Zr for $\text{Ni}_{64.5}\text{Zr}_{35.5}$. In spite of some differences between calculated MD simulations and experimental data, the peaks of Ni-Ni and Ni-Zr around $q = 3 \text{ (\AA}^{-1}\text{)}$ corresponding to the dominant SRO clusters in $\text{Ni}_{64.5}\text{Zr}_{35.5}$ only have some minor deviations.

also enclosed by ten triangles, which form the surface of a half slightly distorted icosahedron. Similarly, the intertwined-cube motif can be regarded as two interpenetrating cubes $C1$ and $C1'$ sharing a common (111) plane as shown in Fig. 4(b). Thus the center Ni atom in intertwined-cube cluster is surrounded by 6 faces (11 atoms), which form two groups of nearly orthogonal squares. By contrast, ICO-like clusters in our MD samples (not shown) are nearly identical to the ideal ICO motif, with only slightly distortions.

After identifying the dominant structure motifs in the glass sample, we take these three motifs along with some common crystalline motifs such as bcc, fcc, and hcp motifs as templates and perform cluster-template alignment for all the Ni-centered clusters extracted from the MD samples to calculate the alignment scores distribution against these templates. Since no dominant motif of Zr-centered clusters is found by the pairwise alignment method other than Z15 and Z16, and the coordination number of Zr in our sample is about 15.6, we only include the common motifs Z15 and Z16 clusters as templates to analyze the SRO of Zr-centered clusters. Figures 5(a) and 5(b) show the distribution of alignment scores for Ni- and Zr-centered clusters from MD glass sample at 300 K, respectively. As shown in Fig. 5(a), compared to the other motifs of Ni-centered cluster, the distribution of scores for mixed-ICO-cube, intertwined-cube, and ICO-like motifs have relatively larger portion in the region with small score. It indicates that the local structures in the sample can be better described by these motifs than the others. Similarly, Fig. 5(b) shows the Z15 cluster is the major motif of Zr-centered cluster in $\text{Ni}_{64.5}\text{Zr}_{35.5}$.

To describe the SRO of glass sample quantitatively, we use an alignment score 0.15 as a cutoff to assign the clusters to the given template. If a cluster has an alignment score less than 0.15 for more than one template, the lowest alignment score

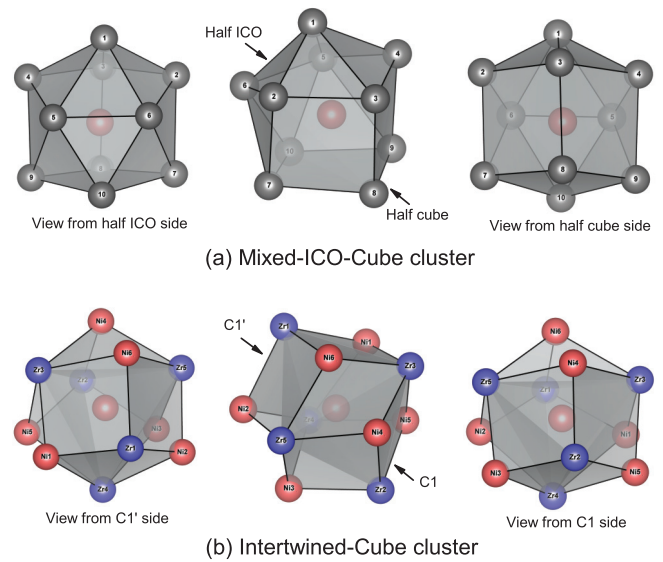


FIG. 4. Two kinds of dominant clusters extracted from the $\text{Ni}_{64.5}\text{Zr}_{35.5}$ glass sample at 300 K by the pairwise alignment method. (a) Mixed-ICO-cube cluster can be viewed as the combination of a half-cube and a half-icosahedron surface. The sites (2, 3, 8, 7), (3, 4, 9, 8), and (7, 8, 9, 10) form three nearly orthogonal squares, respectively. The other portions of surfaces are ten triangles constituting a slightly distorted half-ICO. (b) Intertwined-cube cluster can be viewed as two interpenetrating cubes with common (111) plane formed by sites (Zr3, Zr4, Zr5). The sites (Ni3, Ni4, Ni5, Zr2, Zr3, Zr4, Zr5) and (Ni1, Ni2, Ni6, Zr1, Zr3, Zr4, Zr5) form the two half-cubic surfaces $C1$ and $C1'$, respectively. Here, the usage of Ni or Zr as the site's name is to imply that the corresponding sites could be mostly occupied by Ni or Zr as revealed in the following investigation.

is used to assign the motif of the cluster. The choice of cutoff value of 0.15 for determining the fraction of the SRO motif is a bit arbitrary but it is guided by considering the thermal motion of the atoms at given temperature. This cutoff value is inferred from the width of the first peak in the calculated pair correlation $g(r)$, which reflects the atomic displacements due to thermal motion. At 300 K, the width of the first peak of $g(r)$ is roughly $0.15 d_0$, where d_0 is the averaged nearest-neighbor bond length.

Table I shows the fractions of SROs in the glass sample at 300 K prepared by continuous cooling of 10^{10} K/s. As a result, we found that the fractions of Ni-centered mixed-ICO-cube, intertwined-cube, and ICO-like motifs in the $\text{Ni}_{64.5}\text{Zr}_{35.5}$ glass sample at 300 K are 18.6%, 9.3%, and 11.8% of the total Ni atoms, respectively. By contrast, the fraction of Zr-centered Z15 motif is only about 4.8% of total Zr atoms. Other kinds of Ni (Zr) centered motifs such as bcc, fcc, and hcp have less than 5% of the total Ni (Zr) atoms. Since the populations of these minority motifs are much less than those of the dominant motifs around the Ni central atoms, such minority motifs will be ignored in the following discussions. From the alignment score distributions shown in Fig. 5, we can see that different choice of the cutoff value will change the fraction numbers of the motifs, but the relative ratios among different motifs are not sensitive to the choice of cutoff value as long as this value is reasonably chosen. Therefore our conclusion that the

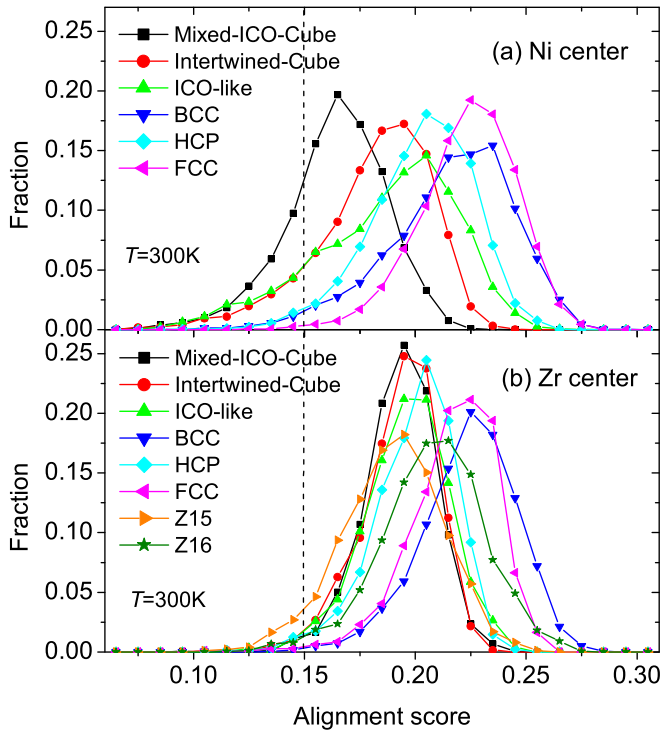


FIG. 5. The distributions of alignment scores against various motifs for (a) Ni- and (b) Zr-centered clusters in the glass sample at 300 K. It can be seen that the score distributions of Ni-centered mixed-ICO-cube, intertwined-cube, and ICO-like motifs have a relatively larger portion in the region of small score, indicating that these three motifs are dominant SRO clusters in $\text{Ni}_{64.5}\text{Zr}_{35.5}$. Choosing a cutoff score value of 0.15, we can obtain that the fractions of mixed-ICO-cube, intertwined-cube, and ICO-like clusters are 18.6%, 9.3%, and 11.8% of the total Ni atoms, respectively.

mixed-ICO-cube, intertwined-cube, and ICO-like motifs are dominating the atomistic SRO in the glassy sample does not depend on the choice of cutoff score.

Moreover, although only about 40% of the Ni atoms can be classified as the central atoms of the three dominant motifs under the cutoff score of 0.15, the total number of atoms involved in the first shells of these dominant clusters is about 95% of the total atoms in the sample. Therefore the local structures in the system are dominated by the Ni-centered mixed-ICO-cube, intertwined-cube, and ICO-like motifs. In fact, if we choose the cutoff value of 0.18 for the Ni-centered clusters, about 86% of Ni atoms can be assigned and the relative ratios among the above three motifs are almost the same as that with the cutoff score of 0.15. The relative fractions of the bcc, fcc, and hcp clusters are still very small. This result indicates that the local orders around the Ni atoms in the glass sample are similar to mixed-ICO-cube, intertwined-cube, and ICO-like clusters.

TABLE I. The fractions of SROs in the glassy sample at 300 K with continuous cooling rate 10^{10} K/s, where the cutoff of alignment score is 0.15.

	bcc	fcc	hcp	Mixed-ICO-cube	ICO-like	Intertwined-cube	Z15	Z16
Ni-centered	0.9%	0.2%	1.2%	18.6%	11.8%	9.3%	N/A	N/A
Zr-centered	0.2%	0.8%	1.5%	1.0%	1.7%	1.0%	4.8%	1.5%

In comparison with the binary $\text{Cu}_{64.5}\text{Zr}_{35.5}$, which has much stronger GFA than $\text{Ni}_{64.5}\text{Zr}_{35.5}$, our MD simulation results show that the fraction of ICO-like cluster in $\text{Ni}_{64.5}\text{Zr}_{35.5}$ is much less than that in $\text{Cu}_{64.5}\text{Zr}_{35.5}$ [38]. It suggests that the ICO cluster indeed plays an important role in glass formation in intermetallic systems. The difference in the ICO fraction in the two systems can be attributed to the strong hybridization between Ni-Zr d electrons, which is much weaker in Cu-Zr systems, as demonstrated by previous *ab initio* MD simulation studies [39,40].

Chemical order is also a useful parameter to describe and predict the GFA in many alloys. To characterize the chemical order in our MD glass samples, all the clusters with the alignment score < 0.15 to a given template are superposed by overlapping the center Ni atoms and keeping the orientation as that at the best alignment position. As shown in Figs. 6(a)–6(c), one can observe that the collective alignment of these clusters gives a pattern of the template, where the red and blue spheres denote Ni and Zr atoms, respectively. In order to calculate the chemical occupation probability, we count the percentage of the Ni and Zr atoms at each site, after all the aligned clusters are overlapped together. Figures 6(d)–6(f) are the calculated occupation probabilities of Ni or Zr on the sites of templates. For mixed-ICO-cube clusters, the atoms 2, 3, 4, 7, 8, 9, and 10 can be counted as cube atoms. Our results show that the chemical composition at sites 2, 4, 8, 10 is Ni-rich (although it is a bit weak in site 8), while at sites 3, 7, 9 is Zr-rich, exhibiting the trend of B2 chemical order. At the other sites of the cluster, Ni and Zr concentrations are close to the stoichiometry of $\text{Ni}_{64.5}\text{Zr}_{35.5}$. This trend of B2 chemical order is even more pronounced in the intertwined-cube clusters as shown in Figs. 6(b) and 6(e). The weaker chemical order in the mixed-ICO-cube motif as compared to that in the intertwined-cube motif would be due to the mix of ICO structure in the mixed-ICO-cube motif. By contrast, the Ni and Zr concentrations at each site of the ICO-like clusters are close to the stoichiometry of $\text{Ni}_{64.5}\text{Zr}_{35.5}$, as one can see from Figs. 6(c) and 6(f). From this analysis, we can see that all the sites with pronounced chemical order are associated with the cubic corners of templates. These sites with excellent chemical order can be viewed as the “genes” of crystalline phase. The emergence of such crystalline genes even when the sample is quenched at very fast cooling rates could be responsible for the weak GFA in the $\text{Ni}_{64.5}\text{Zr}_{35.5}$ sample.

We also examined the MRO around the mixed-ICO-cube and intertwined-cube SRO clusters. By overlapping the center atoms of the same SRO clusters and keeping the orientation of the clusters at the positions from the SRO alignment with a given template, we can see the alignment distribution of the atoms in the second shell of these clusters. As shown in Fig. 7(a), we can see that the atoms in the second shell of the mixed-ICO-cube clusters resemble the B2 structure. In particular, one can observe that the second shell sites are mostly

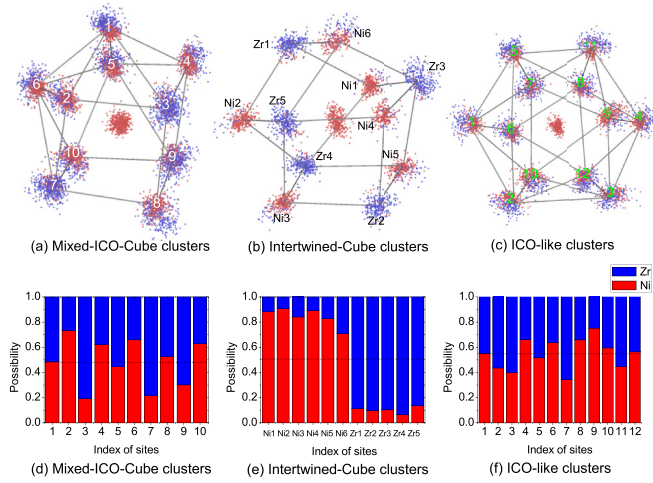


FIG. 6. The atomic configurations of collective alignment for (a) mixed-ICO-cube, (b) intertwined-cube, and (c) ICO-like clusters, where the red and blue sphere denote Ni and Zr atoms, respectively. The possibility of each site being Ni (red) or Zr (blue) is also shown in (d)–(f), where the dashed lines denote the averaged possibilities. In the cubic part of mixed-ICO-cube clusters, the chemical composition at sites 2, 4, 8, 10 is Ni-rich (although it is a bit weak in site 8) while at sites 3, 7, 9 is Zr-rich, exhibiting the trend of B2 chemical order. This trend of B2 chemical order is even more pronounced in the intertwined-cube clusters. Our results demonstrate that the crystallinelike clusters have much more pronounced chemical order than that of ICO, implying that the crystalline phase could still emerge in the $\text{Ni}_{64.5}\text{Zr}_{35.5}$ sample even by the fast cooling process.

occupied by Ni atoms, indicating excellent chemical order of B2 crystal fragment. Similarly, the atoms of the second shell around the intertwined-cube cluster centers are also arranged in a bcc-like lattice, as shown in Fig. 7(b). Like in the case of mixed-ICO-cube motif, we found that the majority of the atoms around these bcc-lattice sites in the second shell of intertwined-cube clusters are Ni. These MRO results demonstrate a certain degree of crystal nucleation ability from the mixed-ICO-cube and intertwined-cube cluster, suggesting the suppression of glass phase formation in the $\text{Ni}_{64.5}\text{Zr}_{35.5}$ sample.

Recently, it has been demonstrated that performing MD simulated annealing below but close to the glass transition temperature (i.e., sub- T_g annealing) can accelerate structural relaxation since the structural relaxation and glass formation is much more efficient in the vicinity of T_g [38,41,42]. To investigate the effects of sub- T_g annealing in Ni-Zr systems, the initial $\text{Ni}_{64.5}\text{Zr}_{35.5}$ sample at 2000 K is continuously cooled down to 925 K at 10^{10} K/s, then the as-quenched sample is annealed for 1400 ns at 925 K. Finally, the annealed sample was continuously cooled down to 300 K at 10^{10} K/s. The MD steps used for such a cooling-annealing-cooling cycle is equivalent to a cooling rate of 1.08×10^9 K/s. Figure 8(a) shows the potential energy at 300 K for different cooling rates including the result from the sub- T_g annealing cycle. It can be seen that the potential energy for the samples with continuous cooling linearly depends on the logarithm of cooling rates, which is similar to the case of other binary alloy systems such as Cu-Zr [41], Al-Sm [42], and Ni-Nb [43]. When considering the error bar of the fitting, the potential energy for $\text{Ni}_{64.5}\text{Zr}_{35.5}$

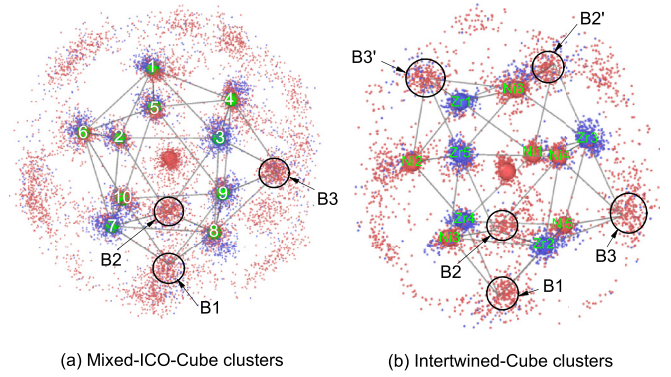


FIG. 7. The atomic configurations of collective alignment of (a) mixed-ICO-cube clusters and (b) intertwined-cube clusters with the second shell atoms. For mixed-ICO-cube clusters, one can see that there are accumulations of the second shell atoms (mostly Ni, red sphere) around the B1, B2, and B3 positions which can be viewed as three nearly bcc centers. It suggests that the half-cubic part of mixed-ICO-cube cluster has the trait of metastable B2 phase in the Ni-Zr system. Similar to the case of mixed-ICO-cube clusters, for intertwined-cube clusters, the possibility of finding a Ni atom around the bcc centers (B1, B2, B3, B2', B3') of two interpenetrating cubes (C1, C1') is relatively large, also implying the existence of a metastable B2 phase in $\text{Ni}_{64.5}\text{Zr}_{35.5}$.

from the sub- T_g annealing simulation is actually not far away from the extrapolation of the least-square fitting line based on the energies of the continuously cooled samples. This result suggests that in order to get the same potential energy, the simulation time used for sub- T_g annealing is almost the same as that used in continuously cooling. This result is very different from the case of a strong glass forming system like $\text{Cu}_{64.5}\text{Zr}_{35.5}$, where the sub- T_g annealing approach can help to speed up the glass formation process [41]. Our results indicate that in a weak glass forming system like the present case of $\text{Ni}_{64.5}\text{Zr}_{35.5}$, sub- T_g annealing is not very effective owing to the relatively stronger crystalline nucleation tendency.

To study the influence of cooling rate on the SRO clusters, we show the fractions of mixed-ICO-cube, intertwined-cube, and ICO-like clusters in the sample of 300 K with different cooling rates in Fig. 8(b). When the cooling rate is lowered, the fraction of ICO-like clusters is nearly constant while that of intertwined-cube clusters increases considerably. The fraction of the mixed-ICO-cube clusters also increases slightly with lowering the cooling rate. The open symbols shown in Fig. 8(b) are the fractions of SRO clusters for the samples after the sub- T_g annealing process with an effective cooling rate of 1.08×10^9 K/s. Since the intertwined-cube cluster has the character of a crystalline phase while the ICO-like cluster is more related to a glass phase, our results suggest that even in the very fast quench process the crystalline phase motifs are still the dominant SRO in the $\text{Ni}_{64.5}\text{Zr}_{35.5}$ system. Therefore $\text{Ni}_{64.5}\text{Zr}_{35.5}$ should not be a good glass former.

To further investigate the competition among different SRO motifs, we also examine the evolution of SRO clusters during the sub- T_g annealing at 925 K. During the annealing process, for every 200 ns, the sample is quenched to 10 K to obtain the inherent structure for SRO analysis. Figure 8(c) shows the evolution of fractions of mixed-ICO-cube, intertwined-cube, and

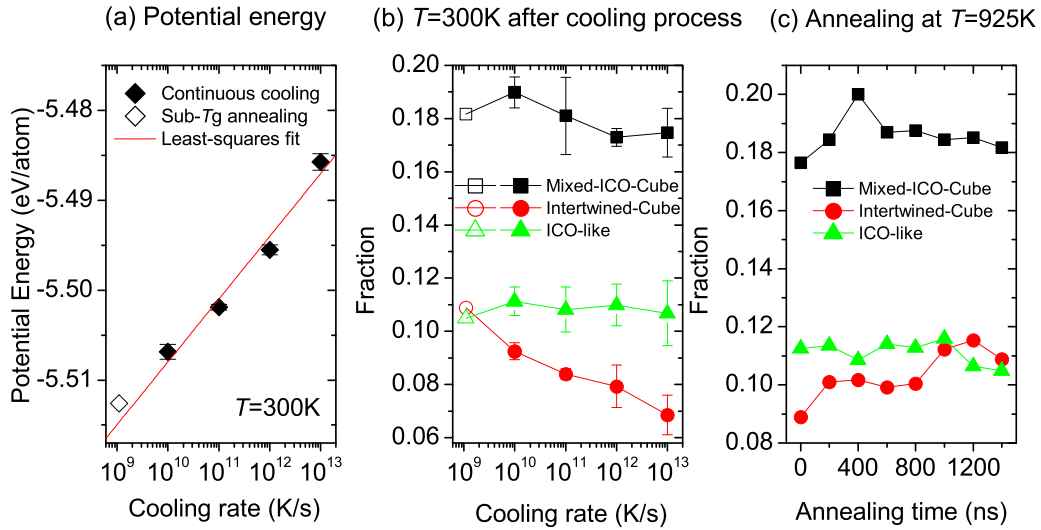


FIG. 8. (a) The potential energy of $\text{Ni}_{64.5}\text{Zr}_{35.5}$ at 300 K for different cooling rates. (b) The fractions of mixed-ICO-cube, intertwined-cube, and ICO-like clusters in $\text{Ni}_{64.5}\text{Zr}_{35.5}$ at 300 K for different cooling rates. With lower cooling rate, the fraction of the intertwined-cube cluster that represents a crystalline phase increases while the fraction of ICO-like cluster is nearly constant, suggesting the suppression of the glass phase formation by the competitors (crystalline phase) in the $\text{Ni}_{64.5}\text{Zr}_{35.5}$ sample. (c) The evolution of fractions of mixed-ICO-cube, intertwined-cube, and ICO-like clusters during the annealing process at temperature 925 K. One can observe that there is a clear phenomenon of competition between the representation of crystalline phase (intertwined-cube cluster) and the glass phase (ICO-like cluster).

ICO-like clusters as the function of annealing time at 925 K. One can observe that the fractions of intertwined-cube and ICO-like cluster fluctuate with annealing time. The fraction of the mixed-ICO-cube clusters is high, more than 17% at the beginning of the annealing and increases sharply during the first 400 ns to about 20%, and then reduces to about 18% from 500 to 1200 ns. At the same time, the fraction of the intertwined-cube clusters increases from about 10% to 11% during the last 400 ns of annealing. By tracking the evolution history of dominant motifs during the annealing simulation, we found that the change of fractions is a dynamic process and different types of motifs in the sample can interchange with each other in the process of the simulation. The fractions of mixed-ICO-cube and intertwined-cube clusters as a function of simulation time seen in Fig. 8(c) are a statistical average result at each simulation time. As the annealing time gets longer and longer, more and more clusters are found to transfer into a crystal-like intertwined-cube motif and reduce the GFA in the sample.

IV. CONCLUSIONS

In summary, the atomic structure of $\text{Ni}_{64.5}\text{Zr}_{35.5}$ alloy has been studied by MD simulations combined with the cluster Alignment method analysis. The calculated total structure factors agree well with the XRD and ND scattering experimental data. By pairwise cluster alignment and clique analysis, we found three kinds of Ni-centered motifs are the dominant SRO in the $\text{Ni}_{64.5}\text{Zr}_{35.5}$ sample at 300 K, i.e., mixed-ICO-cube, intertwined-cube, and ICO-like cluster. The mixed-ICO-cube motif has half-ICO and half-cube structure. The intertwined-cube cluster is constituted of two interpenetrating slightly distorted cubes with common (111) plane. The ICO-like cluster is very close to an ideal ICO with slight distortion. Meanwhile, the fractions of the other kinds of

Ni-centered motifs and all Zr-centered motifs are much smaller than those of the above three dominant motifs.

In addition, we also analyze the chemical order of the three dominant SRO clusters by directly evaluating the occurrence probability of Ni (Zr) atoms around each sites of the SRO cluster. Our results show that the cubic portion of mixed-ICO-cube and the whole intertwined-cube clusters have excellent chemical order, implying the emergence of crystalline motifs in the $\text{Ni}_{64.5}\text{Zr}_{35.5}$ alloy even in fast cooled samples. Furthermore, we studied the MRO of the mixed-ICO-cube and intertwined-cube clusters and found that around the bcc centers there is a high probability of finding another Ni atom at the second shell from the central Ni atom. This suggests that the mixed-ICO-cube, intertwined-cube clusters have the character of crystalline a metastable B2 phase in the Ni-Zr system. We also found that the fraction of the intertwined-cube cluster increases with lowering cooling rate while that of the ICO-like cluster remains constant, implying that the glass formation would be suppressed by the small crystalline fragments of the B2 phase. The evolution of SROs with the annealing time also shows competition between intertwined-cube and ICO-like clusters. Our results suggest that the weak GFA can be attributed to the existence of SROs with crystalline character in the $\text{Ni}_{64.5}\text{Zr}_{35.5}$ alloy.

ACKNOWLEDGMENTS

Work at Ames Laboratory was supported by the U.S. Department of Energy (DOE), Office of Science, Basic Energy Sciences, Materials Science and Engineering Division including a grant of computer time at the National Energy Research Scientific Computing Center (NERSC) in Berkeley. Ames Laboratory is operated for the U.S. DOE by Iowa State University under contract No. DE-AC02-07CH11358. L. Tang and Z. J. Yang would like to acknowledge the financial support

from the National Natural Science Foundation of China (Grant Nos. 11304279 and 11104247) and Natural Science Foundation of Zhejiang Province, China (Grant No. LY18E010007). L. Tang also would like to acknowledge the financial support

from China Scholarship Council (No. 201608330083). T. Q. Wen and N. Wang also would like to acknowledge the financial support from the National Natural Science Foundation of China (Grant Nos. 51671160 and 51271149).

- [1] P. Chaudhari and D. Turnbull, Structure and properties of metallic glasses, *Science* **199**, 11 (1978).
- [2] H. S. Chen, Glassy metals, *Rep. Prog. Phys.* **43**, 353 (1980).
- [3] A. L. Greer, Metallic glasses, *Science* **267**, 1947 (1995).
- [4] A. Inoue, Stabilization of metallic supercooled liquid and bulk amorphous alloys, *Acta Mater.* **48**, 279 (2000).
- [5] W. H. Wang, C. Dong, and C. H. Shek, Bulk metallic glasses, *Mater. Sci. Eng. R* **44**, 45 (2004).
- [6] J. Schroers, Processing of bulk metallic glass, *Adv. Mater.* **22**, 1566 (2010).
- [7] M. Chen, A brief overview of bulk metallic glasses, *NPG Asia Mater.* **3**, 82 (2011).
- [8] J. Ding and E. Ma, Computational modeling sheds light on structural evolution in metallic glasses and supercooled liquids, *npj Comput. Mater.* **3**, 9 (2017).
- [9] C. A. Schuh, T. C. Hufnagel, and U. Ramamurty, Mechanical behavior of amorphous alloys, *Acta Mater.* **55**, 4067 (2007).
- [10] K. F. Kelton, G. W. Lee, A. K. Gangopadhyay, R. W. Hyers, T. J. Rathz, J. R. Rogers, M. B. Robinson, and D. S. Robinson, First X-Ray Scattering Studies on Electrostatically Levitated Metallic Liquids: Demonstrated Influence of Local Icosahedral Order on the Nucleation Barrier, *Phys. Rev. Lett.* **90**, 195504 (2003).
- [11] T. Schenk, D. Holland-Moritz, V. Simonet, R. Bellissent, and D. M. Herlach, Icosahedral Short-Range Order in Deeply Undercooled Metallic Melts, *Phys. Rev. Lett.* **89**, 075507 (2002).
- [12] A. Hirata, P. Guan, T. Fujita, Y. Hirotsu, A. Inoue, A. R. Yavari, T. Sakurai, and M. Chen, Direct observation of local atomic order in a metallic glass, *Nat. Mater.* **10**, 28 (2011).
- [13] H. W. Sheng, W. K. Luo, F. M. Alamgir, J. M. Bai, and E. Ma, Atomic packing and short-to-medium-range order in metallic glasses, *Nature* **439**, 419 (2006).
- [14] P. F. Guan, T. Fujita, A. Hirata, Y. H. Liu, and M. W. Chen, Structural Origins of the Excellent Glass Forming Ability of $\text{Pd}_{40}\text{Ni}_{40}\text{P}_{20}$, *Phys. Rev. Lett.* **108**, 175501 (2012).
- [15] F. C. Frank, Supercooling of liquids, *Proc. R. Soc. London, Ser. A* **215**, 43 (1952).
- [16] D. B. Miracle, A structural model for metallic glasses, *Nat. Mater.* **3**, 697 (2004).
- [17] Y. Q. Cheng and E. Ma, Atomic-level structure and structure–property relationship in metallic glasses, *Prog. Mater. Sci.* **56**, 379 (2011).
- [18] A. J. Cao, Y. Q. Cheng, and E. Ma, Structural processes that initiate shear localization in metallic glass, *Acta Mater.* **57**, 5146 (2009).
- [19] Z. Altounian, T. Guo-hua, and J. O. Strom-Olsen, Crystallization characteristics of Ni–Zr metallic glasses from $\text{Ni}_{20}\text{Zr}_{80}$ to $\text{Ni}_{70}\text{Zr}_{30}$, *J. Appl. Phys.* **54**, 3111 (1983).
- [20] Z. Altounian and J. O. Strom-Olsen, Superconductivity and spin fluctuations in M –Zr metallic glasses ($M = \text{Cu}, \text{Ni}, \text{Co}, \text{and Fe}$), *Phys. Rev. B* **27**, 4149 (1983).
- [21] K. H. J. Buschow, Short-range order and thermal stability in amorphous alloys, *J. Phys. F: Met. Phys.* **14**, 593 (1984).
- [22] T. Abe, M. Shimono, M. Ode, and H. Onodera, Estimation of the glass forming ability of the Ni–Zr and the Cu–Zr alloys, *J. Alloys Compd.* **434–435**, 152 (2007).
- [23] D. Wang, Y. Li, B. B. Sun, M. L. Sui, K. Lu, and E. Ma, Bulk metallic glass formation in the binary Cu–Zr system, *Appl. Phys. Lett.* **84**, 4029 (2004).
- [24] Y. Li, Q. Guo, J. A. Kalb, and C. V. Thompson, Matching glass-forming ability with the density of the amorphous phase, *Science* **322**, 1816 (2008).
- [25] T. Fukunaga, K. Itoh, T. Otomo, K. Mori, M. Sugiyama, H. Kato, M. Hasegawa, A. Hirata, Y. Hirotsu, and A. C. Hannon, Voronoi analysis of the structure of Cu–Zr and Ni–Zr metallic glasses, *Intermetallics* **14**, 893 (2006).
- [26] I. Kaban, P. J  v  ri, V. Kokotin, O. Shuleshova, B. Beuneu, K. Saksl, N. Mattern, J. Eckert, and A. L. Greer, Local atomic arrangements and their topology in Ni–Zr and Cu–Zr glassy and crystalline alloys, *Acta Mater.* **61**, 2509 (2013).
- [27] S. R. Wilson and M. I. Mendelev, Anisotropy of the solid–liquid interface properties of the Ni–Zr B33 phase from molecular dynamics simulation, *Philos. Mag.* **95**, 224 (2015).
- [28] S. Plimpton, Fast parallel algorithms for short-range molecular dynamics, *J. Comput. Phys.* **117**, 1 (1995).
- [29] X. W. Fang, C. Z. Wang, Y. X. Yao, Z. J. Ding, and K. M. Ho, Atomistic cluster alignment method for local order mining in liquids and glasses, *Phys. Rev. B* **82**, 184204 (2010).
- [30] Y. Sun, F. Zhang, Z. Ye, Y. Zhang, X. Fang, Z. Ding, C.-Z. Wang, M. I. Mendelev, R. T. Ott, M. J. Kramer, and K.-M. Ho, ‘Crystal genes’ in metallic liquids and glasses, *Sci. Rep.* **6**, 23734 (2016).
- [31] D. G. Quirinale, G. E. Rustan, S. R. Wilson, M. J. Kramer, A. I. Goldman, and M. I. Mendelev, Appearance of metastable B2 phase during solidification of $\text{Ni}_{50}\text{Zr}_{50}$ alloy: Electrostatic levitation and molecular dynamics simulation studies, *J. Phys.: Condens. Matter* **27**, 085004 (2015).
- [32] T. E. Faber and J. M. Ziman, A theory of the electrical properties of liquid metals, *Philos. Mag.* **11**, 153 (1965).
- [33] D. Waasmaier and A. Kirfel, New analytical scattering-factor functions for free atoms and ions, *Acta Crystallogr.* **51**, 416 (1995).
- [34] V. F. Sears, Neutron scattering lengths and cross sections, *Neutron News* **3**, 26 (1992).
- [35] M. I. Mendelev, F. Zhang, Z. Ye, Y. Sun, M. C. Nguyen, S. R. Wilson, C. Z. Wang, and K. M. Ho, Development of interatomic potentials appropriate for simulation of devitrification of $\text{Al}_{90}\text{Sm}_{10}$ alloy, *Modell. Simul. Mater. Sci. Eng.* **23**, 045013 (2015).
- [36] F. Zhang, Y. Sun, Z. Ye, Y. Zhang, C.-Z. Wang, M. I. Mendelev, R. T. Ott, M. J. Kramer, Z.-J. Ding, and K.-M. Ho, Solute–solute correlations responsible for the prepeak in structure factors of undercooled Al-rich liquids: A molecular dynamics study, *J. Phys.: Condens. Matter* **27**, 205701 (2015).

- [37] T. Q. Wen, L. Tang, Y. Sun, K. M. Ho, C. Z. Wang, and N. Wang, Crystal genes in a marginal glass-forming system of $\text{Ni}_{50}\text{Zr}_{50}$, *Phys. Chem. Chem. Phys.* **19**, 30429 (2017).
- [38] Y. Zhang, F. Zhang, C.-Z. Wang, M. I. Mendelev, M. J. Kramer, and K.-M. Ho, Cooling rates dependence of medium-range order development in $\text{Cu}_{64.5}\text{Zr}_{35.5}$ metallic glass, *Phys. Rev. B* **91**, 064105 (2015).
- [39] L. Huang, C. Z. Wang, S. G. Hao, M. J. Kramer, and K. M. Ho, Atomic size and chemical effects on the local order of Zr_2M ($M = \text{Co}, \text{Ni}, \text{Cu}$, and Ag) binary liquids, *Phys. Rev. B* **81**, 014108 (2010).
- [40] Y. Huang, L. Huang, C. Z. Wang, M. J. Kramer, and K. M. Ho, Comparative study of local atomic structures in $\text{Zr}_2\text{Cu}_x\text{Ni}_{1-x}$ ($x = 0, 0.5, 1$) metallic glasses, *J. Appl. Phys.* **118**, 195902 (2015).
- [41] F. Zhang, M. I. Mendelev, Y. Zhang, C.-Z. Wang, M. J. Kramer, and K.-M. Ho, Effects of sub- T_g annealing on $\text{Cu}_{64.5}\text{Zr}_{35.5}$ glasses: A molecular dynamics study, *Appl. Phys. Lett.* **104**, 061905 (2014).
- [42] Y. Sun, Y. Zhang, F. Zhang, Z. Ye, Z. Ding, C.-Z. Wang, and K.-M. Ho, Cooling rate dependence of structural order in $\text{Al}_{90}\text{Sm}_{10}$ metallic glass, *J. Appl. Phys.* **120**, 015901 (2016).
- [43] Y. Zhang, R. Ashcraft, M. I. Mendelev, C. Z. Wang, and K. F. Kelton, Experimental and molecular dynamics simulation study of structure of liquid and amorphous $\text{Ni}_{62}\text{Nb}_{38}$ alloy, *J. Chem. Phys.* **145**, 204505 (2016).